CrystEngComm

PAPER

View Article Online
View Journal | View Issue

Cite this: *CrystEngComm*, 2025, **27**, 5819

Cu- and Zn-based 1D MOFs as hosts to encapsulate Eu(III) for tuning white light emission†

Palak Chaudhary,[a] Sahil Thakur,[ab] Raghubir Singh*[b] and Varinder Kaur*[a]

Received 28th April 2025,
Accepted 9th July 2025

DOI: 10.1039/d5ce00448a

rsc.li/crystengcomm

In this work, the synthesis of luminescent Eu(III)-encapsulated Cu MOF and Zn MOF is reported as efficient materials with tunable light-emitting properties. The MOFs were derived from a salen-type Schiff base with multiple N donors and additional –OH groups for holding Eu(III). The Eu(III)-encapsulated MOFs, Eu–Cu MOF and Eu–Zn MOF hybrids, were characterized using FTIR, TGA, PXRD, FE-SEM, and XPS analyses. The hybrids emitted a wide range of light in the visible and near-IR range. The International Commission on Illumination (CIE) coordinates of Eu–Cu MOF and Eu–Zn MOF hybrids were (0.25, 0.35) and (0.31, 0.29), with correlated colour temperature (CCT) magnitudes of 9896 K and 6719 K, respectively. Additionally, when the outer epoxy resin layer of LEDs was uniformly coated with Eu–Cu MOF and Eu–Zn MOF, green light and near-white light were emitted, respectively, at a voltage of 3 V. Thus, this work provides a new synthetic approach for the development of white light-emitting host–guest materials.

1. Introduction

Metal–organic frameworks (MOFs) have been widely explored as solid supports for hosting guests in various fields like heterogeneous catalysis,[1] gas capture/separation,[2] sensing,[3] ion exchange[4] and luminescence[5] owing to their ordered structures, appropriate pore sizes, chemical and thermal stabilities, and tunability of organic skeletons.[6] Their photoluminescent properties make them suitable materials for the fabrication of single-component optoelectronic devices,[7] laser diodes,[8] light-emitting diodes (LED),[9,10] and ultra-violet (UV) photodetectors.[11] White light-emitting diodes (WLEDs) are the most economical lighting sources, providing high energy efficiency, increased brightness, a longer lifespan and low-temperature performance; therefore, they have successfully replaced traditional incandescent bulbs and fluorescent lamps in modern lighting and visual display systems.[12,13] The traditional methods for fabricating WLEDs include blending multiple LEDs (red, green, and blue) or coating a blue LED with a yellow phosphor; however, their different decay rates reduce the light efficiency. Additionally, their high correlated colour temperature (CCT) and low color rendering index (CRI) values affect their overall performance.[14–16] Previously, inorganic–organic porous hybrids such as pristine MOFs, namely, $[Cd(tzphtpy)_2]_n{\cdot}6.5nH_2O$ {Htzphtpy = 4-(tetrazol-5-yl)phenyl-2,2′:6′,2″-terpyridine},[10] $[Ba(2,6\text{-ndc})(H_2O)_2{\cdot}H_2O]$ {2,6-ndc = 2,6-naphthalenedicarboxylate},[17] and $[Pb_2(pia)_2(DMA){\cdot}DMA]$ {H_2pia = 5-(pyridin-4-yl)isophthalic acid and DMA = *N*,*N*-dimethylacetamide},[18] and rare-earth-metal-encapsulated MOFs, namely, [EuTb@dlMOF]{dlMOF = Zn(μ-L)(μ-bidpe), bidpe = 4,4′-bis(imidazol-1-yl)diphenyl ether, H_2L = biphenyl-3,5-dicarboxylic acid}[19] and Eu@UiO66-AB {AB = 4-acetylbenzoic acid},[20] have been reported for fabricating WLEDs. These materials require specialized synthetic conditions, including high temperatures, extended reaction times, and complex fabrication strategies.[10,17–20] Moreover, MOFs such as Eu@MIL-53(Al)-AB {AB = 4-acetyl benzoic acid},[20] $[Eu_4(obb)_6(H_2O)_9{\cdot}(H_2O)]$ {H_2obb = 4,4′-oxybisbenzoic acid}[21] and Zn-IPA MOF {IPA = isophthalic acids}[22] are unable to emit white light with the desired CIE coordinate (x = 0.33, y = 0.33).

Transition metal coordination frameworks exhibit photoluminescence in a specific range of the visible spectrum; however, the introduction of a guest chromophore can make these materials multi-wavelength emitters.[23] Notably, lanthanide-incorporated frameworks show improved white light emission, narrow emission band, significant antenna-generated shift, multiband emission, and excellent luminescence efficiency owing to the antenna effect of ligands.[24] Earlier, some aromatic N-heterocycles (including imidazole, pyrrole, pyrimidine, pyridine, and their derivatives) and multifunctional carboxylic acids have been utilized to construct MOFs for light-emitting applications.[25]

[a] *Department of Chemistry, Panjab University, Sector-14, Chandigarh-160014, India. E-mail: var_ka04@yahoo.co.in, var_ka04@pu.ac.in*
[b] *Department of Chemistry, DAV College, Sector 10, Chandigarh-160011, India. E-mail: raghu_chem2006@yahoo.com, raghubirsingh@davchd.ac.in*

† Electronic supplementary information (ESI) available: Characterization data of all the compounds, elemental mapping, XPS spectra, PXRD pattern of Cu MOF, Zn MOF, Eu-Cu MOF, Eu-Zn MOF. Crystallographic data and structural parameters; crystallographic data are comprised in the CCDC codes of 2444353 (Zn MOF) and 2444361 (Cu MOF). For ESI and crystallographic data in CIF or other electronic format see DOI: https://doi.org/10.1039/d5ce00448a

The N-based ligands contribute substantially to the photoluminescence of complexes, driving the excitation spectrum from the ultraviolet to the near-infrared or visible region and providing a high coordination affinity towards metal centres. It is well known that the Zn^{2+} ions show a great tendency to coordinate with N donor ligands and display an extra edge for inducing photoluminescence properties due to the d^{10} system.[26] Here, we report the synthesis of high-quality crystalline 1D Zn-MOF and Cu-MOF under mild reaction conditions using an N-equipped compartmental ligand. This ligand possesses some interesting chemical properties and binding behaviour due to the presence of the –OH functional group. The –OH group exhibits variable binding modes; it divides the N⁀N⁀O⁀N⁀N donor set into two compartments and can hold two metal ions in separate compartments or it protrudes outward leaving the N⁀N⁀N⁀N donor set for coordinating a single metal ion in the compartment. Earlier, the inward orientation of the –OH groups has been reported to hold Dy^{3+} and Cu^{2+} ions, thus producing dinuclear complexes.[27,28] In contrast, the formation of mononuclear complexes has been observed with Mn^{2+} and Cu^{2+}, indicating the non-involvement of –OH due to its outward orientation.[29,30] In another case, the Cu complex was extended to a 1D coordination polymer by the involvement of chlorate ions as bridges.[30] The presence of –OH has also been reported to enhance the overall activity of the molecule and facilitate Schiff base cyclization of the ligand in the presence of Fe(II), which induces the oxidative DNA cleavage activity in the molecule.[31] In the current work, the –OH acts as an additional active site for holding Eu(III) ions within the channels formed by 1D Zn-MOF and Cu-MOF. The Eu(III)-encapsulated MOFs produced near-white light and greenish light emissions in the Eu–Zn MOF and Eu–Cu MOF hybrids, respectively, demonstrating their potential for application in optical devices. The host–guest combination of hybrids results in reduced molecular vibration, which diminishes non-radiative relaxation and thus improves multiband emission efficiency.[32] Moreover, to verify the physical significance of the synthesized material, a prototype was developed by coating Eu–Cu MOF and Eu–Zn MOF on the plastic epoxy resin cover of LEDs. The fabrication of Eu(III)-encapsulated MOFs provides an alternative way for constructing efficient optoelectronic devices.

2. Experimental

2.1 Materials and methods

All experiments were carried out using standard apparatus and commercially available chemicals. The chemicals, 2-pyridinecarboxaldehyde (ALS Chemicals, India), 1,3-diaminopropan-2-ol (BLD Pharm, India), sodium sulphate (Avra, India), zinc(II) nitrate hexahydrate (SRL, India) and cupric(II) nitrate trihydrate (SRL, India), and europium(III) chloride hexahydrate (Sigma-Aldrich, India), were procured in high purity. The solvents *N*,*N*-dimethylformamide, methanol, ethanol, hexane, and dichloromethane were purchased from Finar, India, and were dried using standard procedures.[33]

2.2 Instrumentation

The FT-IR spectra were recorded using a Perkin Elmer Spectrum Two spectrometer. The solution-phase NMR spectra (^{1}H NMR, ^{13}C NMR) were recorded using a BRUKER AVANCE 500-NMR spectrometer. Mass spectrometric measurements were performed using a VG Analytical (70-S) spectrometer and Waters XEVO G2-XS QTOF mass spectrometer. Single crystals of compounds were diffracted using a Bruker D8 SMART APEX2 CMOS diffractometer with Mo Kα radiation (λ = 0.71073 Å). The crystal structures were solved using the Olex2 software, the intrinsic phasing method of the ShelXT structure solution program. Powder X-ray data was obtained using Panalytical's X'Pert Pro. Scanning electron microscopy (SEM) images for detailed information on surface morphology were obtained from FEI Nova SEM-450 at 10 kV and FESEM, ZEISS, and ULTRA PLUS. XPS analysis was carried out on a Thermo Scientific NEXSA surface analyzer and Thermo Fisher Scientific NEXSA photoemission spectrometer. For recording fluorescence spectra, a Shimadzu Fluorescence RF-6000 spectrometer equipped with a glass cell was used. The absorption spectra were obtained *via* a Jasco V-530 UV-vis spectrometer. The thermogravimetric analysis experiments were performed by an SDTQ600 (V20.9 Build 20) instrument (Artisan Technology Group, Champaign, IL) under a nitrogen atmosphere. The colour emission of MOFs was determined using the CIE chromaticity diagram 1931.

2.3 Synthetic procedures

2.3.1 Schiff base (SB). The Schiff base (SB) was synthesized by a slight modification of an earlier reported method.[30] In a double-neck round-bottom flask, 1,3-diaminopropan-2-ol (5.55 mmol, 0.5 g) and 2-pyridinecarboxaldehyde (11.10 mmol, 1.054 mL) were dissolved in dry dichloromethane (50 mL), and the mixture was stirred in the presence of anhydrous Na_2SO_4 for 4 h. Sodium sulphate was filtered, and the solvent was evaporated under a vacuum to afford a yellow oil. The oil was then dissolved in 50 mL of methanol, and the contents were further heated to reflux for 24 h. The solvent was removed under reduced pressure using a rotary evaporator, which afforded SB as a yellow oil. The product was washed with diethyl ether and hexane to remove the impurities.

Yield: 75% (1.12 g); FT-IR (ATR) cm^{-1}: 3371 (broad O–H), 2910 (C–H), 1648 (C=N), 1581 (C=$N_{pyridine}$), 1431 (C–C), 1088 (C–O), 763 (C–H bending). ^{1}H NMR (500 MHz, DMSO-d_6): δ (ppm) 3.68 (2H, m, H^{2b}), 3.86 (2H, m, H^{2a}), 4.10 (1H, m, H^1), 4.93 (alc OH, broad singlet), 7.46 (2H, m, H^7), 7.88 (2H, m, H^6), 7.99 (2H, dt, ^3J = 5 Hz, H^5), 8.36 (2H, s, H^3), 8.65 (2H, dq, ^3J = 5 Hz, H^8); ^{13}C NMR (125 MHz, DMSO-d_6): δ (ppm) 64.8 (C^2), 69.5 (C^1), 120.4 (C^5), 124.9 (C^7), 136.7 (C^6), 149.2 (C^8), 154.1 (C^3), 162.9 (C^4); ESI-MS (*m*/*z*): 271.08 $[L + 3H]^+$, 285.09 $[L + NH_3/ OH^•]^+$, 181.06 $[C_9H_{15}N_3O]^+$.

2.3.2 Synthesis of Cu MOF. The Cu MOF was synthesized by mixing a methanolic solution of SB (0.559 mmol, 0.15 g) with a methanolic solution of cupric nitrate trihydrate (0.559 mmol, 0.13 g), making the total solution volume 25 mL. The contents were heated to reflux for 8 h, followed by solvent evaporation under vacuum to afford a blue powder. The powdered product was dissolved in dimethylformamide and kept for crystallization using a diffusion method in diethyl ether. Blue needle-shaped crystals suitable for single-crystal X-ray diffraction were obtained.

Yield (crystals): 53% (0.15 g), melting point: 222–224 °C; FT-IR (ATR) cm^{-1}: 3259 (broad O–H), 1660 (C═N), 1605 (C═$N_{pyridine}$), 1378 (C–C), 1302 (C–N), 1049 (N–O), 780 (C–H bend), 644 (Cu–N), 568 (Cu–$N_{pyridine}$). ESI-MS (*m*/*z*): 331.05 $[M + H]^+$.

2.3.3 Synthesis of Zn MOF. The synthesis of Zn MOF was performed in the same manner as discussed above by reacting SB (0.559 mmol, 0.15 g) and zinc nitrate hexahydrate (0.559 mmol, 0.16 g) in methanol. The product was obtained as a brown powder, which yielded pale yellow needle-shaped crystals by the diffusion method in dimethylformamide and diethyl ether. Yield (crystals): 51% (0.15 g), melting point: 255–256 °C, FT-IR (ATR) cm^{-1}: 3384 (broad O–H), 1653 (C═N), 1596 (C═$N_{pyridine}$), 1401 (C–C), 1294 (C–N), 1022 (N–O), 776 (C–H bend), 639 (Zn–N), 505 (Zn–$N_{pyridine}$). ^{1}H NMR (500 MHz, DMSO-d_6): δ (ppm) 4.15 (2H, m, H^{2b}), 4.25 (1H, m, H^1), 4.33 (2H, d, ^3J = 15 Hz, H^{2a}), 5.32 (alc OH, s), 8.00 (2H, t, $^3J_{6-5}$ = 10 Hz, $^3J_{6-7}$ = 15 Hz, H^6), 8.18 (2H, d, $^3J_{5,6}$ = 10 Hz, H^5), 8.43 (2H, t, $^3J_{7-8}$ = 5 Hz, $^3J_{7-6}$ =15 Hz, H^7), 8.85 (2H, s, H^3), 9.0 (2H, d, $^3J_{8-7}$ = 4 Hz, H^8); ^{13}C NMR (125 MHz, DMSO-d_6): δ (ppm) 75.8 (C^2), 88.3 (C^1), 128.4 (C^5), 146.2 (C^7), 146.9 (C^6), 149.3 (C^8), 152.9 (C^3), 163.2 (C^4); ESI-MS (*m*/*z*): 340.45 $[M–OH + Na + H]^+$.

2.4 Encapsulation of Eu in Cu MOF and Zn MOF

The encapsulation of Eu in Cu MOF was achieved by dispersing europium(III) chloride hexahydrate (0.136 mmol, 50 mg) and Cu MOF (50 mg) in the hexane–ethanol mixture (8 : 2 v/v). The contents were stirred for 8 h, and the product was centrifuged at 15 000 rpm for 5 min. The resulting solid was washed with ethanol and dried in an oven for 2 h. A sky-blue powder was collected as the product Eu–Cu MOF. The encapsulation of Eu in Zn MOF was carried out similarly using europium(III) chloride hexahydrate (0.136 mmol, 50 mg) and Zn MOF (50 mg), which yielded the product Eu–Zn MOF as a light-yellow powder.

Eu–Cu MOF. Yield: 62% (62 mg), melting point: 222–224 °C, FT-IR (ATR) cm^{-1}: 3340 (broad O–H), 1635 (C═N), 1599 (C═$N_{pyridine}$), 1450 (C–C), 1294 (C–N), 1025 (N–O), 797 (C–H bend), 738 (Eu–O), 631 (Cu–N), 504 (Cu–$N_{pyridine}$).

Eu–Zn MOF. Yield: 71% (71 mg), melting point: 256–258 °C FT-IR (ATR) cm^{-1}: 3320 (broad O–H), 1650 (C═N), 1588 (C═$N_{pyridine}$), 1443 (C–C), 1291 (C–N), 1014 (N–O), 768 (C–H bend), 740 (Eu–O), 631 (Zn–N), 501 (Zn–$N_{pyridine}$).

3. Results and discussion

3.1 Synthesis and characterization

The ligand SB was synthesized through the Schiff base condensation reaction of 1,3-diaminopropan-2-ol and 2-pyridinecarboxaldehyde using a reported method with slight modifications.[28] It involves reacting 1,3-diaminopropan-2-ol and 2-pyridinecarboxaldehyde at room temperature in the presence of a desiccant (anhydrous Na_2SO_4), followed by the reaction of SB with cupric nitrate trihydrate and zinc nitrate hexahydrate, yielding Cu MOF and Zn MOF, respectively (Scheme 1).

The FT-IR spectrum of the SB ligand shows a broad band at 3371 cm^{-1} due to O–H stretching, two sharp bands at 1648 cm^{-1} and 1581 cm^{-1} due to two types of C═N stretching vibrations (azomethinic C═N and C═$N_{pyridine}$), and a sharp band at 1431 cm^{-1} due to C–C stretching (ESI,† Fig. S1). The C═N band centred at 1648 cm^{-1} in the free ligand is shifted to 1660 cm^{-1} and 1653 cm^{-1} in Cu MOF and Zn MOF, respectively, due to the formation of the Cu/Zn–N bond. The N–O vibration of nitrate bridges is observed at 1049 cm^{-1} and 1022 cm^{-1} in Cu MOF and Zn MOF, respectively.[34] An additional band at 644 cm^{-1} in Cu MOF and 639 cm^{-1} in Zn MOF confirms the formation of the Cu–N and Zn–N bonds, respectively. The Cu–$N_{pyridine}$ and Zn–$N_{pyridine}$ bond formation is confirmed by the presence of additional bands at 568 cm^{-1} and 505 cm^{-1} in Cu MOF and Zn MOF, respectively.

In the ^{1}H NMR, the SB ligand exhibits a singlet at 8.36 ppm for H^3, at 4.10 ppm for H^1, and two separate signals at 3.68 ppm and 3.86 ppm for H^2 protons due to geminal coupling (ESI,† Fig. S2). In Zn MOF, the doublet of quartets of H^8 merges into a doublet and shifts from 8.65 to 9.00 ppm, the singlet at 8.36 shifts to 8.85 ppm for H^3, the doublet of triplets at 7.99 merges into a doublet and shifts to 8.18 ppm for H^5 (ESI,† Fig. S3). Also, ^{13}C NMR of the SB ligand reveals the presence of C═N at 154.1 ppm and C═N pyridine at 149.2 ppm (ESI,† Fig. S4). In Zn MOF, C═N shifts to 152.9 ppm from 154.1 ppm (ESI,† Fig. S5). The ESI-MS of ligand SB exhibits a molecular ion peak at 271.08 due to $(M + 3H)^+$ and a fragmentation peak at 285.09 corresponding to $[M + NH_3/OH^•]$ (ESI,† Fig. S6). The ESI-MS for Cu MOF and Zn MOF exhibits a peak at 331.05 for $[M + H]^+$ and at 340.45 for $[M–OH + Na + H]^+$, respectively (ESI,† Fig. S7 and S8). The ^{1}H and ^{13}C NMR were not recorded for Cu MOF owing to the very poor solubility and paramagnetic nature of Cu(II). The Cu(II) complexes display broad signals and poor spectral resolution due to the rapid nuclear relaxation of paramagnetic Cu(II) centres.[35]

The structural parameters and binding behaviour of the 1D MOFs differ from most of the previously reported complexes of this ligand. However, they closely resemble the $[Cu(HL)(ClO_4)]$ MOF, where bridges are formed by perchlorate ions.[30] The metal centres are six-coordinate in these MOFs with an N_4O_2 coordination geometry. Here, the Schiff base ligand coordinates with copper and zinc as a tetradentate

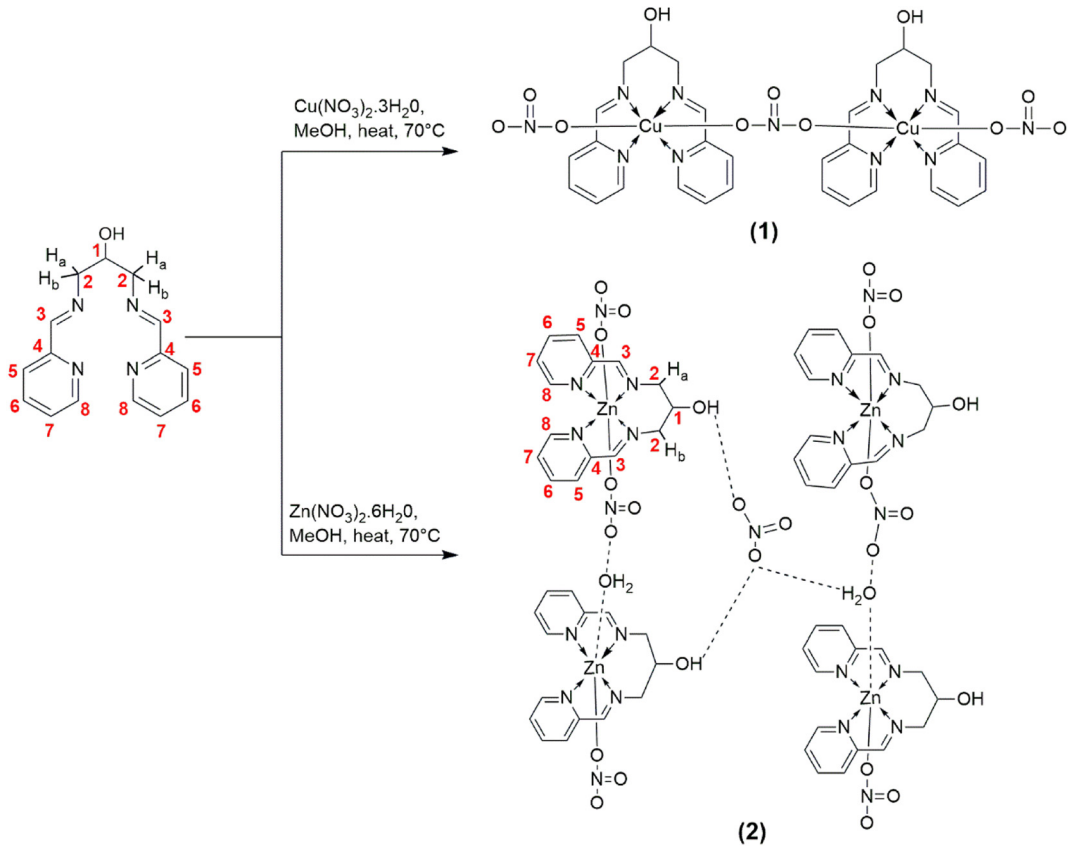

Scheme 1 Schematic for the synthesis of 1) Cu MOF and 2) Zn MOF.

ligand through two pyridine nitrogen atoms and two imine nitrogen atoms. The elongated axial positions are occupied by nitrate ligands. A single-crystal X-ray diffraction analysis reveals that the Cu MOF crystallized in the $P2_1/n$ space group of the monoclinic crystal system. In the structure shown in Fig. 1a, the Cu(II) ion is coordinated with the nitrogen atoms from both imine groups (N2 and N3), the nitrogen atoms from the pyridine rings (N1 and N4), and the oxygen atoms of two nitrate ions, resulting in a distorted octahedral geometry. The bond lengths are found to be Cu–N3 (1.997 Å),

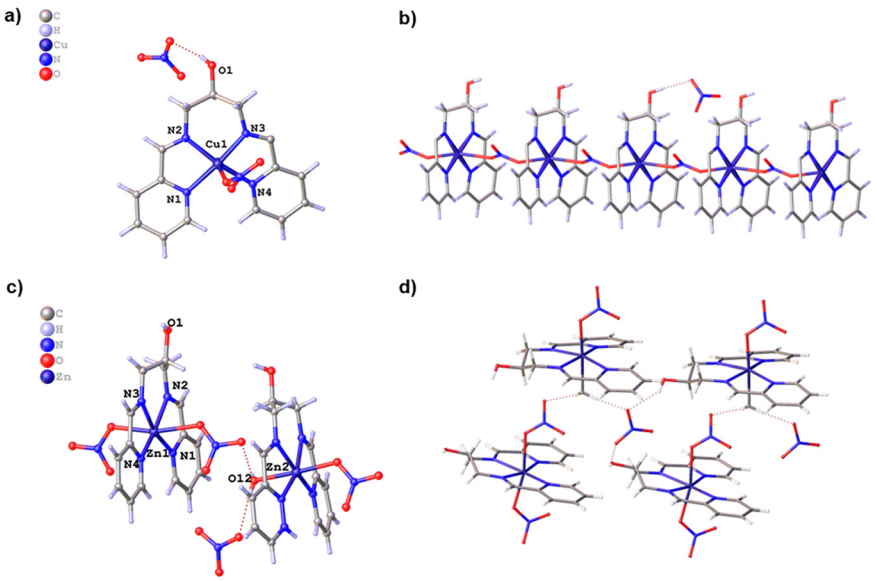

Fig. 1 (a) Asymmetric unit of a Cu MOF, (b) side view of the Cu MOF framework, (c) asymmetric unit of a Zn MOF, and (d) top-down view of the Zn MOF framework.

Cu–N2 (2.004 Å), Cu–N4 (2.079 Å), and Cu–N1 (2.015 Å). The Cu MOF network is further extended by nitrate bridging, with a Cu–O2 bond length of 2.266 Å (Fig. 1b). Similarly, the Zn MOF crystallized in the *P*1 space group of the triclinic crystal system. Its asymmetric unit comprises two distinct Zn(II) ion centres, Zn1 and Zn2, both exhibiting similar coordination with nitrogen atoms from the imine groups (N2 and N3) and the pyridine nitrogen atoms (N1 and N4) as shown in Fig. 1c. Zn1 is coordinated to two nitrate ions, while Zn2 is coordinated to one nitrate ion and one water molecule, resulting in a distorted octahedral geometry at both centres. Additionally, there are nitrate ions present within the lattice, each of which is hydrogen-bonded to a Zn1 centre through an (O1H—O–N, 2.162 Å) interaction and to two Zn2 centres *via* (HO12H—O–N, 2.088 Å) interactions. This unique binding arrangement formed a 1D architecture comprising two parallel chains, one featuring Zn1-bonded molecules and the other containing Zn2-bonded molecules. The hydroxyl group of 1,3-diamino-2-propanol does not participate in binding and remains free with outward orientation from the coordination sphere. This may be due to steric hindrance, electronic factors, or lack of proper orientation for effective binding with metal ions, leading the coordination sphere to involve mainly nitrogen atoms and nitrate ions (Fig. 1d). Crystallographic data and parameters used for structure refinement are given in ESI† Tables S1 and S2 provides information about specific measurements of bond lengths and bond angles.

The presence of a free hydroxyl group with an outward orientation provides an interactive site to hold the metal ions within the 1D layers of MOFs. Thus, Eu(III) ions are embedded on the surface of these MOFs, which form a coating on the surface of the MOFs. The FT-IR spectra of Eu–Cu MOF and Eu–Zn MOF resemble the parent MOFs (Fig. 2a and b). The spectrum of Eu–Cu MOF shows a broad band at 3340 cm^{-1} for O–H stretching, which is probably due to solvated Eu(III) ions. A shifting in the bands for C═N from 1660 cm^{-1} to 1635 cm^{-1}, C═$N_{pyridine}$ from 1605 cm^{-1} to 1599 cm^{-1}, N–O from 1049 cm^{-1} to 1025 cm^{-1},[34] Cu–N from 644 cm^{-1} to 631 cm^{-1}, and Cu–$N_{pyridine}$ from 568 cm^{-1} to 504 cm^{-1} is observed, suggesting the dispersion of Eu(III) ions over the surface of the MOF layers through π-interactions. A similar trend was observed in the case of Eu–Zn MOF, where the broadening of the O–H band is found along with the shifting of bands (C═N from 1653 cm^{-1} to 1650 cm^{-1}, C═$N_{pyridine}$ from 1596 cm^{-1} to 1588 cm^{-1}, N–O peak from 1022 cm^{-1} to 1014 cm^{-1}, Zn–N from 639 cm^{-1} to 631 cm^{-1}, and Zn–$N_{pyridine}$ from 505 cm^{-1} to 501 cm^{-1}). Both Eu–Cu MOF and Eu–Zn MOF retain their characteristic vibrational bands in their FT-IR (ATR) spectra, which account for the stability and integrity of the host frameworks after the infusion of Eu(III) ions in the layers.

The thermal behaviour of Cu MOF, Eu–Cu MOF, Zn MOF, and Eu–Zn MOF was examined by thermogravimetry, and the respective curves are presented in Fig. 3. In Cu MOF, the initial mass loss of 2.80% up to 230 °C is attributed to the escape of solvent and trapped water molecules. When the temperature is increased to 230 °C, a second weight loss of 68.02% is observed due to the breakdown of Cu MOF. The third mass loss of 7% that occurs after the temperature is raised above 235 °C is related to the formation of CuO and Eu_2O_3, resulting from the disintegration of the complete skeleton.[36] Similarly, a large mass loss of 31.7% is observed in the range of 222 °C to 428 °C due to the breakdown of Zn MOF, followed by a mass loss of 13.6% up to 800 °C, attributed to the formation of ZnO. Therefore, the thermal stability of Zn MOF is higher than that of Cu MOF. When evaluating the inclusion of Eu(III) in the system, it is found that Eu–Cu MOF exhibits higher thermal stability than Cu MOF, with a mass loss of 25.4% up to 505 °C due to the breakdown of the host framework, in addition to the release of absorbed solvent molecules. Similarly, Eu–Zn MOF is thermally more stable than Zn MOF, as evidenced by the higher mass loss of 27.4% observed up to 430 °C due to the breakdown of the structure.

In addition, PXRD analysis of Cu MOF and Zn MOF was performed to ensure the purity of the bulk sample, which coincides well with the simulated pattern obtained from single-crystal X-ray diffraction data (ESI,† Fig. S9 and S10). The PXRD pattern of Cu MOF exhibits diffraction peaks at 9.8°, 12.8°, 19.8°, and 25.5° corresponding to the (220), (400), (440), and (040) planes.[37] From the comparison between the X-ray diffraction (PXRD) patterns of Cu MOF and the Eu–Cu MOF, additional diffraction peaks in the latter are identified

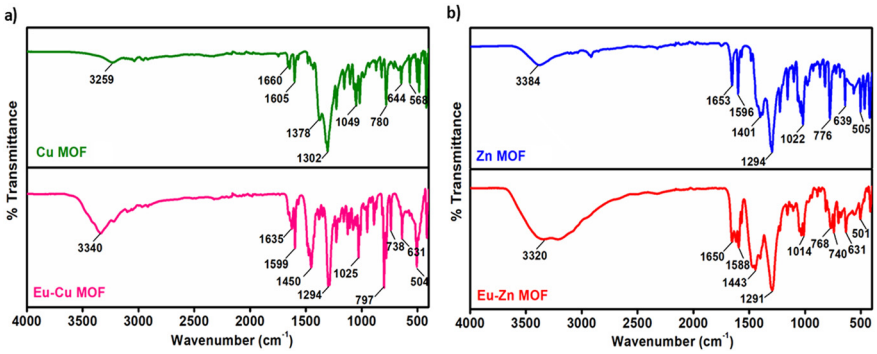

Fig. 2 FT-IR spectra of (a) Cu MOF and Eu–Cu MOF and (b) Zn MOF and Eu–Zn MOF.

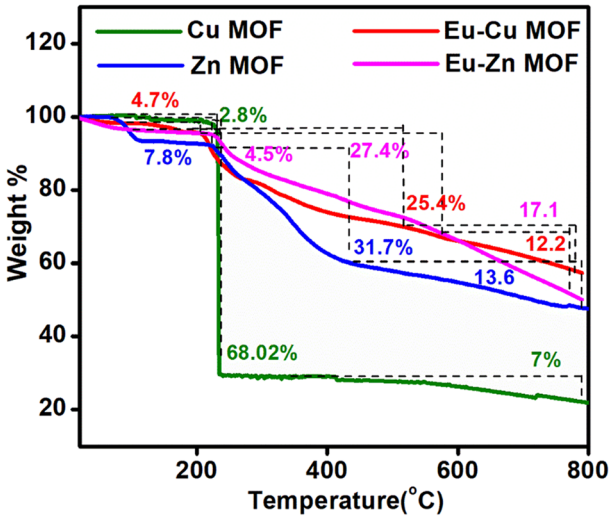

Fig. 3 TGA curves of Cu MOF, Eu–Cu MOF, Zn MOF, and Eu–Zn MOF.

at 10.6°, 18.5°, and 20.2°, along with the characteristic peaks of Cu MOF. These peaks can be tentatively assigned to the (010), (020), and (110) diffraction planes related to Eu(III) inserted into the structure (ESI,† Fig. S11). The PXRD of the Eu–Zn MOF also shows similar peaks at 9.2° and 19.1°, which are tentatively assigned to the (010), (020) diffraction planes, and other peaks at 2θ values of 11.2°, 14.2°, 17.9°, 25.1°, 31.2°, 42.3°, corresponding to the (002), (010), (012), (211), (006), and (008) crystal planes, confirming the presence of ligand-coordinated Eu(III) in the system (ESI,† Fig. S12). These assignments corroborate the reported literature on Eu(III)-infused MOFs with similar environments but different ligand backbones.[38,39]

Surface morphologies of Cu MOF investigated by field-emission scanning electron microscopy (FE-SEM) reveal a flat sheet or film-like morphology of the material; however, deposition of flakes is observed on the flat surface in Eu–Cu MOF after infusion (Fig. 4a–d). Zn MOF also reveals a similar sheet-like morphology and dot-like deposits on the sheets in Eu–Zn-MOF (Fig. 4e–h). Further EDAX analysis and elemental mapping confirmed the presence of Cu, C, O, N and Cu, C, O, N, Eu, Cl as constituent elements in Cu MOF and Eu–Cu MOF, respectively (ESI,† Fig. S13 and S14). Similarly, Zn, C, O, N, and Eu, Cl, Zn, C, O, N were observed as constituent elements in Zn MOF and Eu–Zn MOF, respectively (ESI,† Fig. S13 and S15).

The XPS survey spectra of all the materials support the results of EDAX and the presence of respective elements in Cu MOF, Zn MOF, Eu–Cu MOF, and Eu–Zn MOF (Fig. 5). In Cu MOF, the spin–orbit pairs Cu $2p_{1/2}$ and Cu $2p_{2/3}$ with binding energy peaks at 953.1 eV and 933 eV correspond to the +2 oxidation state with additional satellite peaks at 943.5 eV and 963 eV (ESI,† Fig. S16a). Also, the XPS spectra of C 1s, O 1s, and N 1s of Cu MOF are as expected (ESI,† Fig. S16b–d). The XPS spectra of Eu–Cu MOF show the photoelectron peaks at 1164.1 eV and 1134.6 eV due to the contribution of spin–orbit pairs $3d_{3/2}$ and $3d_{5/2}$, which indicates the successful encapsulation of Eu(III) in the host framework (ESI,† Fig. S17a). In addition, the binding energy peaks observed at 953.4 eV and 933.1 eV correspond to the +2 oxidation state of Cu with additional satellite peaks at 943.3 eV and 963.1 eV (ESI,† Fig. S17b). Eu–Cu MOF also retained the characteristic peaks of Cl 2p, O 1s, N 1s, and C 1s in the Eu–Zn MOF framework (ESI,† Fig. S17c–f). In Zn MOF, the Zn 2p scan shows two major characteristic peaks with binding energies of 1043.1 eV and 1020 eV, attributed to the spin–orbit pairs of $2p_{1/2}$ and $2p_{3/2}$ of Zn^{2+} ions, respectively (ESI,† Fig. S18a). Additionally, the XPS spectra of O 1s, N 1s, and C 1s of Zn MOF are found as expected (ESI,† Fig. S18b–d). The XPS spectra of Eu–Zn MOF show the photoelectron peaks at 1163.3 eV and 1133 eV due to the contribution of spin–orbit pairs $3d_{3/2}$ and $3d_{5/2}$, which indicates the successful encapsulation of Eu(III) in the Eu–Zn MOF framework (ESI,† Fig. S19a). The binding energy peaks at 1043.6 eV and 1020.5 eV, corresponding to the presence of Zn^{2+}, were retained along with the characteristic peaks of Cl 2p, O 1s, N 1s, and C 1s (ESI,† Fig. S19b–f).

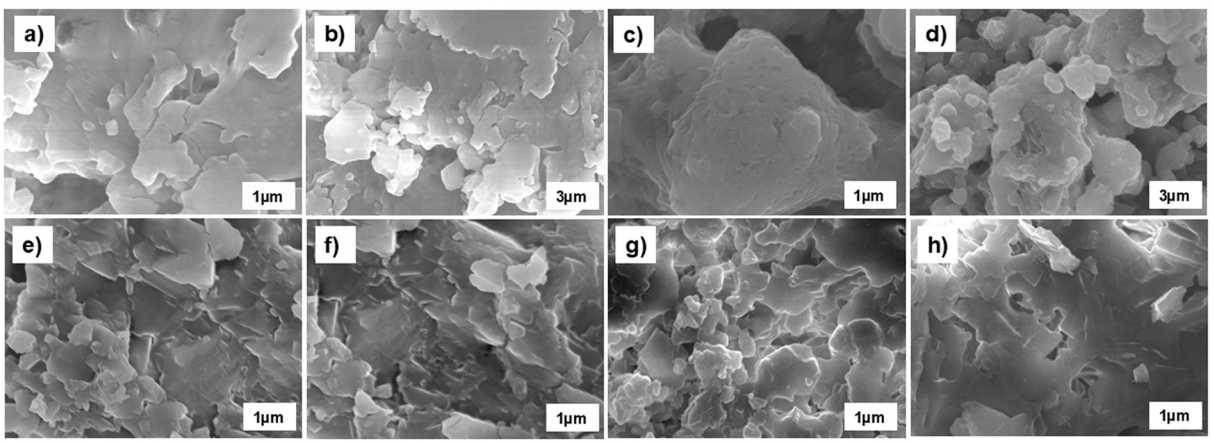

Fig. 4 FE-SEM images of (a and b) Cu MOF, (c and d) Eu–Cu MOF, (e and f) Zn MOF, and (g and h) Eu–Zn MOF.

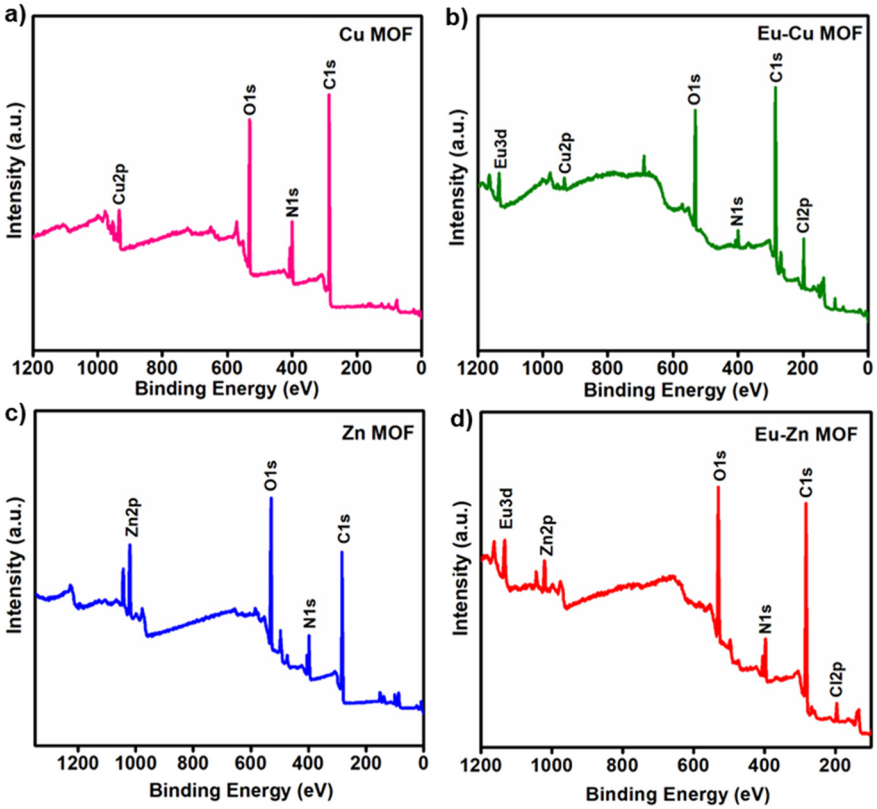

Fig. 5 XPS survey spectra of (a) Cu MOF, (b) Eu–Cu MOF, (c) Zn MOF, and (d) Eu–Zn MOF.

3.2 Photoluminescence studies

The UV-vis absorption spectra were recorded at room temperature in methanol. The SB exhibits absorption bands at 236 nm and 267 nm due to π–π* and n–π* transitions in the ligand. The Cu MOF exhibits absorption bands centred at 216 nm and 288 nm, which can be observed due to ligand-to-ligand charge transfer and ligand-to-metal charge transfer (LMCT). In Eu–Cu MOF, the corresponding bands remain the same with a slight broadening after the deposition of Eu(III) species over the MOF surface. Similarly, Zn MOF exhibits ligand-to-ligand charge transfer and ligand-to-metal charge transfer (LMCT) absorption bands centred at 226 nm and 279 nm with a negligible broadening in Eu–Zn MOF (ESI,† Fig. S20).[40] In both cases, the broadening is not very significant as indicated by the full width at half maximum (FWHM) values of the emission bands (summarized in Table S3†). The slight increase in FWHM from 41.12 nm in Cu MOF to 43.64 nm in Eu–Cu MOF and from 30.08 nm in Zn MOF to 30.69 nm in Eu–Zn MOF confirms a negligible structural distortion after introducing Eu^{3+} ions in the host framework.

The photoluminescence spectra of SB and MOFs were recorded at room temperature in methanol, and the spectra are given in Fig. 6. SB exhibits an emission band centred at 491 nm, and another at higher energy at 457 nm when excited at 400 nm, related to the fluorescence and phosphorescence of this ligand.[41,42] The Cu MOF spectrum displays an emission band centred at 451 nm and another with a maximum at 426 nm, with higher energy, also under excitation at 400 nm, resulting in an emission colour in the blue region, as verified by its CIE coordinate (0.17, 0.12) and CCT magnitude of 3931 K (Fig. 7). Notably, the luminescence of Eu(III) complexes can be sensitized upon the near-visible light excitation (350 nm $< \lambda_{ex} <$ 415 nm) and 465 nm. The emission spectra of Eu–Cu MOF and Eu–Zn MOF were recorded in this range of wavelengths; however, excitations at $\lambda <$ 360 nm and $\lambda >$ 410 nm failed to produce white light emission and gave the perception of blue, turquoise blue, and green for Eu–Cu MOF, and blue, green, and yellow for Eu–Zn MOF, respectively (ESI,† Fig. S21a, b and S22). Therefore, the PL spectra were recorded in the region 370–400 nm, and the best results were obtained at 400 nm.[43] In contrast, in the emission spectrum of Eu–Cu MOF, compared to that of the precursor, the bands in the blue region underwent a bathochromic shift, being now observed at 483 nm and 456 nm, together with the characteristic Eu(III) bands centred at 591 nm ($^5D_0 \rightarrow 323\ ^7F_1$), 617 nm ($^5D_0 \rightarrow {}^7F_2$), 694 nm ($^5D_0 \rightarrow {}^7F_4$). In this case, the visual perception of the emission appears green, with a CIE 1931 coordinate of (0.25, 0.35), CCT magnitude of 9896 K, and CRI value 76 (Fig. 6 and 7). The photoluminescence quantum yield (PLQY) of Eu–Cu MOF calculated using standard rhodamine 6G is found to be 74.4%.[44] However, for the Eu–Cu MOF, the combinations of the emission bands, considering the variation of their relative intensities, did not result in the perception of white light for certain excitation wavelengths.

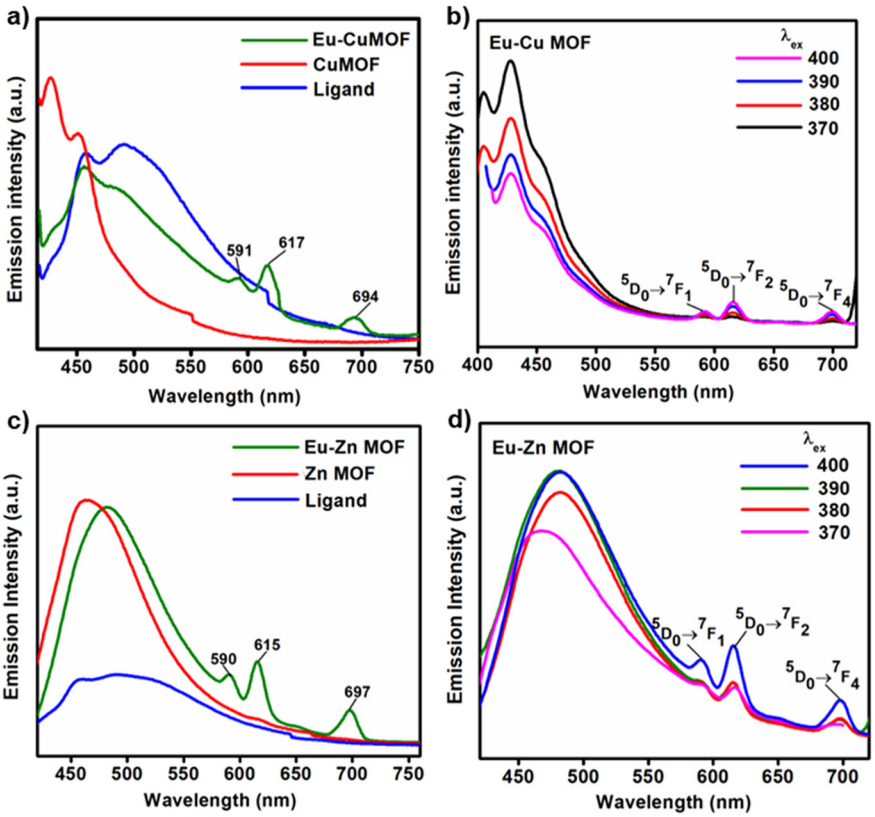

Fig. 6 PL studies at room temperature in methanol. (a) Emission spectra of the SB ligand, Cu MOF, and Eu–Cu MOF at an excitation wavelength of 400 nm, (b) emission spectra of Eu–Cu MOF at different excitation wavelengths (370–400 nm), (c) emission spectra of the SB ligand, Zn MOF, and Eu–Zn MOF at an excitation wavelength of 400 nm, and (d) emission spectra of Eu–Zn MOF at different excitation wavelengths (370–400 nm).

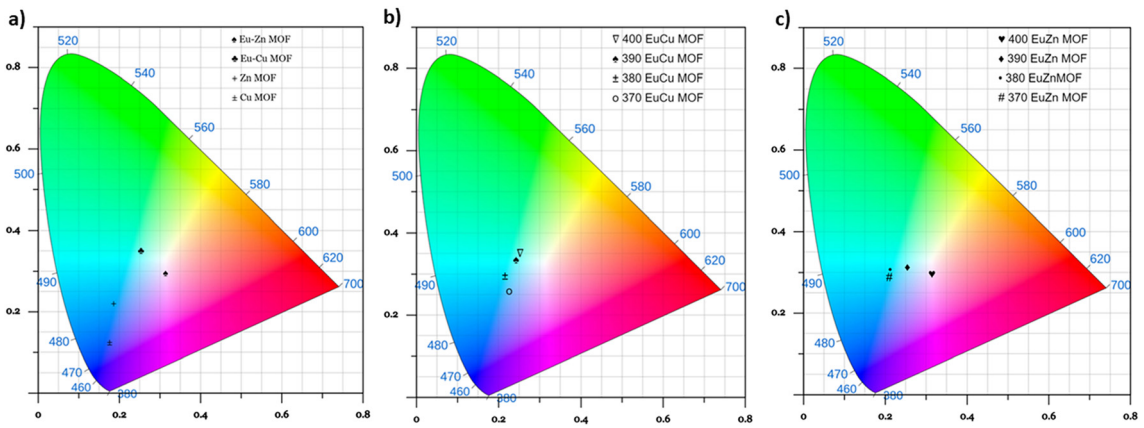

Fig. 7 Chromaticity diagram of (a) Cu MOF, Eu–Cu MOF, Zn MOF, Eu–Zn MOF at an excitation wavelength of 400 nm, (b) Eu–Cu MOF at different excitation wavelengths, and (c) Eu–Zn MOF at different excitation wavelengths.

Zn MOF at the same excitation wavelength of 400 nm shows an emission band centred at 464 nm displaying blue light emission with the CIE coordinate (0.18, 0.22) and the corresponding CCT magnitude of 145 506 K (Fig. 7a). In contrast, Eu–Zn MOF displays a blue colour upon excitation at 370 nm, a turquoise blue colour at 380 and 390 nm, and a near-white light emission at 400 nm (Fig. 7c). The most effective tunability of emission bands was observed at an excitation wavelength of 400 nm, where the intensity of emission bands was the maximum resulting in near white light emission. The spectrum displays emission bands centred at 481 nm, along with characteristic bands due to Eu(III) ions centred at 697 nm ($^5D_0 \rightarrow {}^7F_4$), 615 nm ($^5D_0 \rightarrow {}^7F_2$), 590 nm ($^5D_0 \rightarrow {}^7F_1$) displaying near white light emission with CIE coordinates (0.31, 0.29), a CCT magnitude of 6719 K, and CRI value of 73 and PLQY equal to 84.9% (ref. 44) (Fig. 7a). The CIE coordinates lie close to the NTSC (National Television

Standards Committee) value. However, the CRI values are lower than the ideal threshold (>80) typically desired for high-quality white light applications.

The electronic transition mechanism involved in Eu–Cu MOF and Eu–Zn MOF is due to the narrowed band characteristics of Eu(III) ions observed from its excited level $^5D_0$, which may also be populated by intramolecular energy transfer (IET) *via* the triplet state of the ligand, T_1 {$T_1 \rightarrow$ Eu(III)}, which in turn is the result of the intersystem crossing (ISC) from the singlet state S_1 to T_1 {$S_1 \rightarrow T_1$}, also known as the "antenna effect" (ESI,† Fig. S23).[45] The encapsulated MOFs with donor-type ligands strongly interact with the 4f orbitals of the dopant and provide a rigid structural framework, thereby enhancing charge-transfer (CT) emissions from π-orbitals to 4f orbitals.

Although these materials do not meet this benchmark, the observed CRI values are comparable to those of early-stage phosphor-based systems, indicating the potential for improvement through further material engineering. The observed CRI values may be attributed to an incomplete spectral balance despite europium doping. It is hypothesized that enhancement could potentially be achieved through ligand engineering to broaden the emission profile or by introducing co-ligands with complementary emissive properties. Such modifications may improve spectral coverage and consequently, the CRI, without compromising luminescent performance. As compared to previous reports on Er–Yb-MOF and Er–Eu-MOF by Xu *et al.* and on a high-efficiency perovskite emitter ($Cs_3Cu_2X_5$) (X = Cl, Br, and I) by Chen *et al.*, the current report offers a new class of structurally tunable, ligand-directed white light-emitting materials that operate under low voltages and emit light across a wide spectral range. Although the PLQY of the hybrids is lower than that of $Cs_3Cu_2X_5$ and does not exhibit upconversion like Ln-MOFs, they present a balance of optical tunability, chemical versatility, and ease of synthesis, with potential for further development in single-component white-light applications.[46,47]

3.3 Prototype for developing WLEDs

The quality of light in lighting devices is governed by various factors such as colour, temperature, and CRI.[48] To verify the physical significance of the synthesized material, the plastic epoxy resin cover of the LEDs was coated with Eu–Cu MOF and Eu–Zn MOF, as reported previously.[49] First, 50 mg of Eu–Cu MOF was dispersed in methanol and sonicated for 5 min to produce a gel-like paste; thereafter, the plastic epoxy resin cover of the LED was dipped in this paste to obtain the Eu–Cu MOF-coated LED. Similarly, Eu–Zn MOF was coated on the plastic epoxy resin cover of the LED. A bare LED appears transparent and emits violet light when a voltage of 3.0 V is applied (Fig. 8a and d). However, the surface of the LED coated with Eu–Cu MOF appears green and emits greenish-blue light at 3.0 V (Fig. 8b and e). Besides, the surface of the LED coated with Zn–Eu MOF appears dark yellow and emits well-distributed white light (Fig. 8c and f).

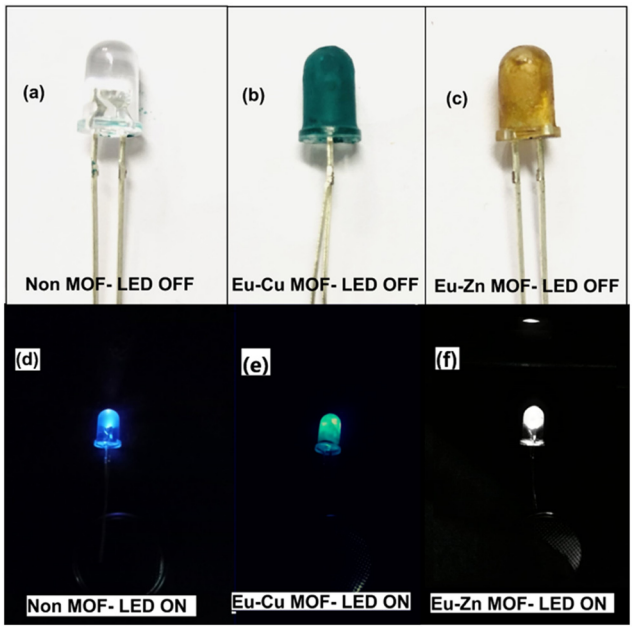

Fig. 8 Display of (a) non-MOF-LED off state, (b) Eu–Cu MOF-LED off state, (c) Eu–Zn MOF-LED off state, (d) non-MOF-LED on state, (e) Eu–Cu MOF-LED on state, and (f) Eu–Zn MOF-LED on state.

To evaluate the emission retention of Eu–Zn MOF, emission spectra of the coated material were recorded after a period of 1, 3, 5, and 7 days. The result shows that all emission bands retain their identity throughout the period, indicating good emission retention (ESI,† Fig. S24). To evaluate the humidity resistance and photostability of Eu–Zn MOF, a coating of the MOF was applied onto the plastic epoxy resin cover of a commercially available LED. The coated LED was exposed to ambient air and continuously operated (switched on) for durations of 1, 2, and 3 days. After each exposure period, the outer MOF coating was analyzed using FTIR spectroscopy to monitor any changes. The FT-IR analysis reveals that the structural framework and chemical composition of the composite remain largely unchanged, thus depicting stability under prolonged light exposure and humid conditions (ESI,† Fig. S25). This method of tuning the properties of MOF with luminescence active centres {Eu(III)} also provides a new direction for the fabrication of high-performance and cost-effective light-emitting devices.

4. Conclusion

In this work, Cu MOF and Zn MOF were constructed from a salen-like ligand and nitrate bridges. They exhibit phenomenal photoluminescence properties. It was found that Cu MOF, on excitation at 400 nm wavelength, emits light in the blue region, whereas Zn MOF emits green light at the same excitation wavelength. Further encapsulation of Eu(III) ions in the host frameworks yields Eu–Cu MOF and Eu–Zn MOF. Enhanced photoluminescence properties result in

white light emission in Eu–Cu MOF and Eu–Zn MOF upon excitation at a 400 nm wavelength, characterized by a low CCT magnitude. To verify the physical significance of the material, a prototype was fabricated by coating the plastic epoxy resin cover of the UV-emitting LED with the Eu(III)-containing materials and it was observed that the Eu–Cu MOF-coated LEDs emit greenish blue light, and Eu–Zn MOF-coated LEDs emit white light; therefore, the materials could be employed in real applications.

Data availability

All the data associated with this research have been presented in the manuscript.

Conflicts of interest

The authors declare that they have no known competing financial interests or personal relationships that could have appeared to influence the work reported in this paper.

Acknowledgements

Authors are grateful to DST-FIST, RUSA, UGC [No. 231610072661] and CSIR [09/0135(18628)/2024-EMR-I] for granting financial support.

References

1 A. Bavykina, *et al.*, Metal–organic frameworks in heterogeneous catalysis: recent progress, new trends, and future perspectives, *Chem. Rev.*, 2020, **120**(16), 8468–8535.
2 Q. Qian, *et al.*, MOF-based membranes for gas separations, *Chem. Rev.*, 2020, **120**(16), 8161–8266.
3 M. Daniel, *et al.*, MOF based electrochemical sensors for the detection of physiologically relevant biomolecules: An overview, *Coord. Chem. Rev.*, 2022, **468**, 214627.
4 A. Kirchon, *et al.*, From fundamentals to applications: a toolbox for robust and multifunctional MOF materials, *Chem. Soc. Rev.*, 2018, **47**(23), 8611–8638.
5 Y. Cui, *et al.*, Luminescent functional metal–organic frameworks, *Chem. Rev.*, 2012, **112**(2), 1126–1162.
6 Q. Wang and D. Astruc, State of the art and prospects in metal–organic framework (MOF)-based and MOF-derived nanocatalysis, *Chem. Rev.*, 2019, **120**(2), 1438–1511.
7 V. Stavila, A. A. Talin and M. D. Allendorf, MOF-based electronic and opto-electronic devices, *Chem. Soc. Rev.*, 2014, **43**(16), 5994–6010.
8 D. Medina-Velazquez, *et al.*, Synthesis of luminescent terbium-thenoyltriflouroacetone MOF nanorods for green laser application, *Opt. Mater.*, 2019, **87**, 3–10.
9 Y. Tang, *et al.*, Luminescent metal–organic frameworks for white LEDs, *Adv. Opt. Mater.*, 2021, **9**(23), 2001817.
10 R. Li, *et al.*, An azole-based metal–organic framework toward direct white-light emissions by the synergism of ligand-centered charge transfer and interligand π–π interactions, *Cryst. Growth Des.*, 2016, **16**(7), 3969–3975.
11 J.-B. Zhang, *et al.*, Metal–Organic Framework-Based Photodetectors, *Nano-Micro Lett.*, 2024, **16**(1), 253.
12 M. Huang, *et al.*, Introduction of multicomponent dyes into 2D MOFs: A strategy to fabricate white light-emitting MOF composite nanosheets, *ACS Appl. Mater. Interfaces*, 2023, **15**(8), 11131–11140.
13 N.-C. Chiu, K. T. Smith and K. C. Stylianou, Metal-organic frameworks for white light emission: From synthesis to device fabrication, *Coord. Chem. Rev.*, 2022, **459**, 214441.
14 H.-Q. Yin and X.-B. Yin, Metal–organic frameworks with multiple luminescence emissions: designs and applications, *Acc. Chem. Res.*, 2020, **53**(2), 485–495.
15 J.-C. Yin, *et al.*, Efficient regulation of energy transfer in a multicomponent dye-loaded MOF for white-light emission tuning, *ACS Appl. Mater. Interfaces*, 2020, **12**(46), 51589–51597.
16 M. Zhu, *et al.*, Designed synthesis, morphology evolution and enhanced photoluminescence of a highly efficient red dodec-fluoride phosphor, Li3Na3Ga2F12: Mn^{4+}, for warm WLEDs, *J. Mater. Chem. C*, 2018, **6**(3), 491–499.
17 S. Kamal, *et al.*, Phosphor-free electrically driven white light emission from nanometer-thick barium–organic framework films, *ACS Appl. Nano Mater.*, 2021, **4**(3), 2395–2403.
18 Z. Yin, *et al.*, Color-tuning and near-sunlight white emission in highly stable rod-spacer MOFs with defective dicubane based lead (II)-carboxyl chains, *Inorg. Chem.*, 2019, **58**(23), 16171–16179.
19 L. Qiu, *et al.*, Tuning the solid-state white light emission of postsynthetic lanthanide-encapsulated double-layer MOFs for three-color luminescent thermometry applications, *Inorg. Chem.*, 2019, **58**(7), 4524–4533.
20 H. S. Jena, *et al.*, White light emission properties of defect engineered metal–organic frameworks by encapsulation of Eu^{3+} and Tb^{3+}, *Cryst. Growth Des.*, 2019, **19**(11), 6339–6350.
21 D. Yang, *et al.*, A series of lanthanide-based metal–organic frameworks: Synthesis, structures, and multicolor tuning of single component, *Inorg. Chem.*, 2017, **56**(4), 2345–2353.
22 Q. Yang, *et al.*, Pressure treatment enables white-light emission in Zn-IPA MOF via asymmetrical metal-ligand chelate coordination, *Nat. Commun.*, 2025, **16**(1), 696.
23 V. W.-W. Yam, A. K.-W. Chan and E. Y.-H. Hong, Charge-transfer processes in metal complexes enable luminescence and memory functions, *Nat. Rev. Chem.*, 2020, **4**(10), 528–541.
24 H. He, *et al.*, Tunable colors and white-light emission based on a microporous luminescent Zn (II)-MOF, *Dalton Trans.*, 2014, **43**(9), 3716–3721.
25 C. Pettinari, A. Tăbăcaru and S. Galli, Coordination polymers and metal–organic frameworks based on poly (pyrazole)-containing ligands, *Coord. Chem. Rev.*, 2016, **307**, 1–31.
26 J. Cepeda and A. Rodríguez-Diéguez, Tuning the luminescence performance of metal–organic frameworks based on d 10 metal ions: from an inherent versatile behaviour to their response to external stimuli, *CrystEngComm*, 2016, **18**(44), 8556–8573.
27 Z. H. Zhu, *et al.*, Temperature-induced formation of two dinuclear dysprosium complexes with different magnetic properties, *Appl. Organomet. Chem.*, 2020, **34**(5), e5622.

28 S. Striegler and M. Dittel, A sugar discriminating binuclear copper (II) complex, *J. Am. Chem. Soc.*, 2003, **125**(38), 11518–11524.
29 M. Mikuriya, H. Fukumoto and T. Kako, Novel dinuclear manganese (II) complexes with monocapped trigonal prism geometries: implication of Mn Mn distance on the catalase activity of dinuclear manganese center, *Inorg. Chem. Commun.*, 1998, **1**(6), 225–227.
30 A. Mukherjee, M. Nethaji and A. R. Chakravarty, Synthesis, crystal structure and imine bond activation of a copper (II) Schiff base complex, *Polyhedron*, 2004, **23**(18), 3081–3085.
31 M. Roy, A. K. Patra, A. Mukherjee, M. Nethaji and A. R. Chakravarty, *Indian J. Chem., Sect. A: Inorg., Bio-inorg., Phys., Theor. Anal. Chem.*, 2007, **46**, 227–237.
32 S. Xing and C. Janiak, Design and properties of multiple-emitter luminescent metal–organic frameworks, *Chem. Commun.*, 2020, **56**(82), 12290–12306.
33 J. Leonard, B. Lygo and G. Procter, *Adv. pract. org. chem.*, CRC press, 2013.
34 A. Joshua, D. DeTata and S. W. Lewis, Source determination of homemade ammonium nitrate using ATR-FTIR spectroscopy, trace elemental analysis and chemometrics, *Forensic Chem.*, 2022, **28**, 100411.
35 N. N. Murthy, *et al.*, NMR and electronic relaxation in paramagnetic Dicopper (II) compounds, *J. Am. Chem. Soc.*, 1997, **119**(9), 2156–2162.
36 J.-J. Cao, *et al.*, A stable Cu-MOF as a dual-functional sensor with high selectivity for fluorescence enhancement and quenching, *J. Solid State Chem.*, 2023, **327**, 124300.
37 J. Cheng, *et al.*, Preparation of a Cu (BTC)-rGO catalyst loaded on a Pt deposited Cu foam cathode to reduce CO_2 in a photoelectrochemical cell, *RSC Adv.*, 2018, **8**(56), 32296–32303.
38 X. He, *et al.*, Facile fabrication of Eu-based metal–organic frameworks for highly efficient capture of tetracycline hydrochloride from aqueous solutions, *Sci. Rep.*, 2023, **13**(1), 11107.
39 S. S. Kolesnik, *et al.*, Ultrasound-assisted synthesis of luminescent micro-and nanocrystalline eu-based mofs as luminescent probes for heavy metal ions, *Nanomaterials*, 2021, **11**(9), 2448.
40 P. Mahata, *et al.*, Luminescent rare-earth-based MOFs as optical sensors, *Dalton Trans.*, 2017, **46**(2), 301–328.
41 X.-G. Yang, *et al.*, Direct White-Light Emitting From a Single Metal–Organic Framework with Dual Phosphorescence Peaks, *Inorg. Chem.*, 2023, **62**(48), 19389–19394.
42 F. Geist, A. Jackel and R. F. Winter, Dual ligand-based fluorescence and phosphorescence emission at room temperature from platinum thioxanthonyl complexes, *Dalton Trans.*, 2015, **44**(9), 3974–3987.
43 J.-M. Li, R. Li and X. Li, Construction of metal–organic frameworks (MOFs) and highly luminescent Eu (III)-MOF for the detection of inorganic ions and antibiotics in aqueous medium, *CrystEngComm*, 2018, **20**(34), 4962–4972.
44 A. M. Brouwer, Standards for photoluminescence quantum yield measurements in solution (IUPAC Technical Report), *Pure Appl. Chem.*, 2011, **83**(12), 2213–2228.
45 S. S. Mohammed Ameen and K. M. Omer, Merging dual antenna effect with target-insensitive behavior in bimetal biligand MOFs to form efficient internal reference signal: color tonality-ratiometric designs, *ACS Mater. Lett.*, 2024, **6**(6), 2339–2349.
46 Y. Chen, *et al.*, Near-Unity PLQY of $Cs_3Cu_2X_5$ (X= Cl, Br) for High-Efficiency White Light-Emitting Diodes with Exceptional Color Quality, *Adv. Mater.*, 2025, 2500083.
47 L. Xu, *et al.*, Dual-mode light-emitting lanthanide metal–organic frameworks with high water and thermal stability and their application in white LEDs, *ACS Appl. Mater. Interfaces*, 2020, **12**(16), 18934–18943.
48 A. Köhnen, *et al.*, Highly color-stable solution-processed multilayer WOLEDs for lighting application, *J. Mater. Chem.*, 2010, **20**(16), 3301–3306.
49 A. G. Bispo-Jr, *et al.*, Recent prospects on phosphor-converted LEDs for lighting, displays, phototherapy, and indoor farming, *J. Lumin.*, 2021, **237**, 118167.